PCCP

PAPER

View Article Online
View Journal | View Issue

Cite this: *Phys. Chem. Chem. Phys.*, 2017, **19**, 31756

Nitrate-assisted photocatalytic efficiency of defective Eu-doped $Pr(OH)_3$ nanostructures†

S. Aškrabić,*[a] V. D. Araújo,[b] M. Passacantando,[c] M. I. B. Bernardi,[d] N. Tomić,[a] B. Dojčinović,[e] D. Manojlović,[f] B. Čalija,[g] M. Miletić[a] and Z. D. Dohčević-Mitrović*[a]

$Pr(OH)_3$ one-dimensional nanostructures are a less studied member of lanthanide hydroxide nanostructures, which recently demonstrated an excellent adsorption capacity for organic pollutant removal from wastewater. In this study, $Pr_{1-x}Eu_x(OH)_3$ (x = 0, 0.01, 0.03, and 0.05) defective nanostructures were synthesized by a facile and scalable microwave-assisted hydrothermal method using KOH as an alkaline metal precursor. The phase and surface composition, morphology, vibrational, electronic and optical properties of the as-prepared samples were characterized by X-ray diffraction (XRD), X-ray photoelectron spectroscopy (XPS), inductively coupled plasma optical emission spectrometry (ICP-OES), transmission electron microscopy (TEM), field emission scanning electron microscopy (FE-SEM), Raman, infrared (IR), photoluminescence (PL), and diffuse reflectance spectroscopy (DRS). It was deduced that the incorporation of Eu^{3+} ions promoted the formation of oxygen vacancies in the already defective $Pr(OH)_3$, subsequently changing the $Pr(OH)_3$ nanorod morphology. The presence of KNO_3 phase was registered in the Eu-doped samples. The oxygen-deficient Eu-doped $Pr(OH)_3$ nanostructures displayed an improved photocatalytic activity in the removal of reactive orange (RO16) dye under UV-vis light irradiation. An enhanced photocatalytic activity of the Eu-doped $Pr(OH)_3$ nanostructures was caused by the synergetic effect of oxygen vacancies and Eu^{3+} (NO_3^-) ions present on the $Pr(OH)_3$ surface, the charge separation efficiency and the formation of the reactive radicals. In addition, the 3% Eu-doped sample exhibited very good adsorptive properties due to different morphology and higher electrostatic attraction with the anionic dye. $Pr_{1-x}Eu_x(OH)_3$ nanostructures with the possibility of tuning their adsorption/photocatalytic properties present a great potential for wastewater treatment.

Received 12th May 2017,
Accepted 6th November 2017

DOI: 10.1039/c7cp06440c

rsc.li/pccp

Introduction

Nanocrystalline rare earth hydroxides have started to draw attention in the recent years because they are relatively facile to synthesize and usually do not require high-temperature annealing. As all rare earth compounds, lanthanide hydroxides display an interesting catalytic, optical, magnetic and adsorptive properties.[1–5] They also represent a straightforward approach for obtaining rare earth oxides since these hydroxides can be transformed to the corresponding oxides by annealing at higher temperatures. Rare earth hydroxides in the form of one-dimensional nanostructures were synthesized by different methods such as precipitation, hydrothermal or microemulsion method or electrodeposition.[2–9] It is known that lanthanide hydroxides most often crystallize into one-dimensional (1D) structures, such as nanorods, nanobundles or nanobelts. These 1D porous structures have the potential for applications in water pollutant removal since their dimensionality makes them much more accessible to the pollutant molecules. Moreover, it is expected that the abundance of –OH groups (inherent in these materials) can have a significant impact on their photocatalytic and adsorptive properties. As the 1D nanostructures are expected to have a better surface activity if the total surface

[a] *Center for Solid State Physics and New Materials, Institute of Physics Belgrade, University of Belgrade, Pregrevica 118, 11080 Belgrade, Serbia. E-mail: sonask@ipb.ac.rs, zordoh@ipb.ac.rs*
[b] *Unidade Acadêmica do Cabo de Santo Agostinho, Universidade Federal Rural de Pernambuco, Cabo do Santo Agostinho, PE, Brazil*
[c] *Department of Physical and Chemical Sciences, University of L'Aquila, Via Vetoio, 67100 Coppito L'Aquila, Italy*
[d] *Instituto de Física de São Carlos, Universidade de São Paulo, São Carlos, SP, Brazil*
[e] *Center of Chemistry, Institute of Chemistry, Technology and Metallurgy, University of Belgrade, Njegoševa 12, 11000 Belgrade, Serbia*
[f] *Faculty of Chemistry, University of Belgrade, Studentski trg 12-16, 11000 Belgrade, Serbia*
[g] *Faculty of Pharmacy, University of Belgrade, Vojvode Stepe 450, 11221 Belgrade, Serbia*

† Electronic supplementary information (ESI) available. See DOI: 10.1039/c7cp06440c

to volume ratio is higher, it is of interest to obtain nanorods/nanowires with a high length-to-diameter ratio. The 1D geometry (the aspect ratio of longer to shorter dimension) can be tuned in the hydrothermal synthesis process by changing the molar ratios of $[OH^-]/[Ln^{3+}]$, where OH^- ions originate from the hydroxide precursor and Ln^{3+} ions from lanthanide salt or oxide, but this ratio is also dependent on the choice of alkaline metal hydroxide. In the case of $Eu(OH)_3$, it was shown that with increasing ratio of $[OH^-]/[Eu^{3+}]$, the aspect ratio of the 1D nanostructures decreased when NaOH was used,[4] but increased when KOH was used.[10]

Among nanocrystalline lanthanide hydroxides, the electrochemically prepared 1D $Pr(OH)_3$ nanostructures were shown to possess the excellent adsorptive properties regarding the dye removal from water.[6,7] Electrodeposition was also used to produce the 1D $Pr(OH)_3$ nanostructures that demonstrated good adsorption of phosphates.[8] Furthermore, the 1D porous $Pr(OH)_3$ nanowire bundles synthesized by a template-free electrochemical deposition method demonstrated good ferromagnetic properties.[2] In addition, the toxicity studies of the porous $Pr(OH)_3$ nanostructures demonstrated their great potential as the environmentally friendly adsorbent materials.[7]

There are only a few papers dedicated to the investigation of the 1D $Pr(OH)_3$ nanostructures[2,6–9] and a majority of them concerned the adsorptive properties of this material. To the best of our knowledge, the photocatalytic properties of pure or doped $Pr(OH)_3$ have not been investigated up till date. This is probably due to the relatively large band gap of these materials (4.7 eV) and their consequent insufficient efficiency in the absorption of the solar radiation. However, a recent study by Dong *et al.*[3] showed that oxygen vacancies can create the electronic states within the band gap of $La(OH)_3$ nanorods, extending their photoresponse range and making them very efficient photocatalysts. In addition, doping of $La(OH)_3$ nanorods with lanthanides, Ln^{3+}, drastically improved their photocatalytic activity; Eu^{3+} was one of the dopants that produced the best results in this direction.[11]

In this study, $Pr(OH)_3$ nanorods and $Pr_{1-x}Eu_x(OH)_3$ (x = 0.01, 0.03, and 0.05) nanostructures were obtained by a microwave-assisted hydrothermal method. We demonstrated that Eu doping influences the changes in the $Pr(OH)_3$ morphology, the adsorption affinity, and can substantially increase the photocatalytic activity of $Pr(OH)_3$ nanorods towards the dye degradation. In addition, the doping changes the content of oxygen vacancies, which, together with synthesis-introduced nitrates and morphology, determine whether the resulting nanostructures are dominantly photocatalysts or adsorbents. The facile and scalable synthesis, the high photocatalytic activity of Eu-doped $Pr(OH)_3$ nanostructures and the possibility of tuning the ratio of their adsorptive/photocatalytic activity present a great potential for their application in the efficient and cost-effective pollutant removal.

Experimental

Preparation of pure and Eu-doped $Pr(OH)_3$ nanostructures

$Pr_{1-x}Eu_x(OH)_3$ (x = 0, 0.01, 0.03, and 0.05) nanostructures were prepared by the microwave-assisted hydrothermal method from the precursor oxides, Pr_6O_{11} and Eu_2O_3. The synthesis procedure included the following steps: first, the precursors were dissolved in aqueous HNO_3; subsequently, 0.02 mol of the dissolved Pr- and Eu-precursors (0, 1%, 3% and 5% at. Eu) were added into 50 mL of distilled water. Following this, 50 mL of a 10 M KOH solution was added rapidly under vigorous stirring. KOH was chosen as a precursor for the hydrothermal synthesis of pure and doped $Pr(OH)_3$ nanorods in this study, as it has been shown that it enhances the formation of 1D nanorods with a higher ratio of length to diameter.[10] The mixed solution was placed in a 110 mL Teflon autoclave (filling 90% of its volume), which was sealed and placed in a microwave-assisted hydrothermal system; 2.45 GHz of microwave radiation was applied at a maximum power of 800 W. The temperature was measured with a temperature sensor (type K thermocouple) inserted into the vessel. Each of the as-prepared solutions was subjected to the microwave hydrothermal synthesis and heated to a temperature of 140 °C for 10 min. The products were then air-cooled to room temperature. The as-obtained precipitate powder was washed several times with distilled water and isopropyl alcohol and then dried on a hot plate at 60 °C for 24 h.

Characterization

The powder X-ray diffraction (XRD) characterization was performed using a Shimadzu diffractometer (Model XRD-7000, CuKα radiation (λ = 1.54 Å), 40 kV and 30 mA). The scanning range was between 5 and 120° (2θ) with a step size of 0.02° and a step time of 5.0 s. The Rietveld analysis was performed using the Rietveld refinement program GSAS.[12] A pseudo-Voigt profile function was used. The specific surface area (S_{BET}) was estimated from the N_2 adsorption/desorption isotherms at liquid nitrogen temperature following the multipoint BET procedure using a Micromeritics ASAP 2000. The determination of the concentrations of europium in the doped samples was performed by inductively coupled plasma optical emission spectrometry (ICP-OES) using an iCAP 6500 Duo ICP (Thermo Fisher Scientific, Cambridge, UK) spectrometer and RACID86 charge injector device (CID) detector with iTEVA operational software. The quantification of europium in the solutions was performed at the following emission wavelength: Eu II 381.967 nm. The morphology of the nanostructures was characterized by transmission electron microscopy (TEM) and field emission scanning electron microscopy (FE-SEM). The TEM characterization was conducted on a Philips CM 300 microscope operating at 300 kV. The SEM measurements were carried out on a Tescan MIRA3 field emission gun at 10–20 kV under high vacuum. The SEM working distance was between 3.3 and 4 mm. The room-temperature micro-Raman spectra of $Pr_{1-x}Eu_x(OH)_3$ nanostructures were excited using solid state Nd:YAG laser line of 514 nm. Low laser power (~2 mW) was applied to prevent the thermal degradation of the sample. Tri Vista 557 triple spectrometer coupled to the nitrogen-cooled CCD detector was employed for the spectra collection at room temperature. X-ray photoelectron spectroscopy (XPS) measurements were performed using the PHI ESCA system equipped with a non-monochromatic Al X-ray source (1486.6 eV) with a hemispherical analyzer. The infrared transmission spectra (IR) were obtained on a Thermo

Nicolet 6700 Fourier transform infrared spectrophotometer at room temperature. Diffuse reflectance spectra (DRS) were acquired using a Specord M40 Carl Zeiss spectrometer. The room-temperature PL measurements were performed on a Spex Fluorolog spectrofluorometer using a 340 nm excitation wavelength.

Photodegradation tests

The photocatalytic activity of $Pr_{1-x}Eu_x(OH)_3$ nanostructures under UV light irradiation was evaluated by monitoring the decomposition of reactive orange (RO16) as a model pollutant. The batch-type experiments were performed in an open thermostated cell (at 25 °C) equipped with a water circulating jacket to maintain the solution at room temperature. A mercury lamp (125 W) was used as a light source. The initial concentration of RO16 in an aqueous suspension was 50 mg L^{-1} and the working volume was 25 mL. Before the photocatalytic experiment, the cell was kept in dark for 60 min in order to achieve the adsorption–desorption equilibrium. At regular time intervals, the aliquots were taken and the dye concentration was monitored by measuring the variation of the intensity of absorption peak at λ_{max} = 494 nm using a Varian Super Scan 3 UV-vis spectrophotometer. The photocatalytic experiments were conducted at the natural pH of the RO16 dye (pH = 4.7). In order to detect the formation of the photogenerated hydroxyl radicals ($OH^{\bullet}$), the photoluminescence (PL) measurements were performed using terephthalic acid, which is known to react with $OH^{\bullet}$ radicals and produce highly fluorescent 2-hydroxyterephthalic acid. The experiment was conducted at ambient temperature and the photocatalyst was placed in an open thermostated cell filled with 20 mL of 5×10^{-4} mol L^{-1} terephthalic acid in a diluted NaOH aqueous solution with a concentration of 2×10^{-3} mol L^{-1}. A UV light source was used and a sampling was performed after 5, 10, and 15 min. The PL spectra of the reaction solution, using an excitation wavelength of 315 nm, were measured on a Spex Fluorolog spectrofluorometer system following the changes of the PL peak at 425 nm, at which the 2-hydroxyterephthalic acid exhibits an intense PL peak.

Results and discussion

The structural characterization of the obtained $Pr_{1-x}Eu_x(OH)_3$ (x = 0, 0.01, 0.03, and 0.05) nanostructures was performed using XRD analysis and the diffraction patterns are shown in Fig. 1. All diffraction peaks of the as-synthesized samples can be perfectly indexed to the hexagonal $P6_3/m$ space group (ICSD No. 200487 or JCPDS No. 83-2304).[13] The secondary peaks (marked with (*) in Fig. 1) at 23.5°, 33.9° and 43.7° were detected in the Eu-doped samples and ascribed to KNO_3 that was formed from the precursors.[14] The lattice parameters (a and c) and oxygen occupancy factor (O_{occup}) calculated from the Rietveld refinement and the quality factors (R_{exp} and R_{Bragg}) of the refinement are summarized in Table 1.

The lattice parameters slightly decreased with Eu doping due to the substitution of the larger Pr^{3+} ion (radii = 1.179 Å) by the smaller Eu^{3+} ion (radii = 1.12 Å)[15] except for the 3% Eu-doped sample. The decrease in O_{occup} with Eu doping signifies an increase in oxygen vacancy content. From Table 1, it can be seen that the 3% Eu-doped sample has the smallest O_{occup}, *i.e.*, the highest content of oxygen vacancies, the presence of which can be responsible for the observed lattice expansion in this sample.[16] In Table 1, the BET specific surface area and the density of the as-synthesized samples are also presented. Clearly, the specific surface area (S_{BET}) decreased in the doped samples compared to that of the pure hydroxide and was the lowest in the 3% Eu-doped sample.

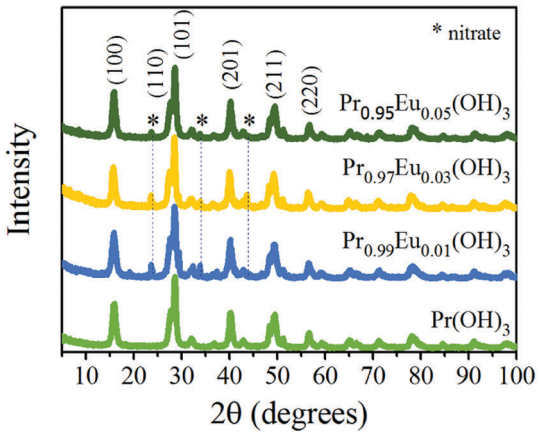

Fig. 1 XRD patterns obtained for $Pr_{1-x}Eu_x(OH)_3$ nanostructures ($0 \leq x \leq 0.05$). The positions of the diffraction peaks assigned to KNO_3 are marked with asterisks.

Table 1 Specific surface area (S_{BET}), lattice parameters (a) and (c), oxygen occupancy factor (O_{occup}), and density (ρ) of $Pr_{1-x}Eu_x(OH)_3$ nanostructures

Sample	S_{BET} (m^2 g^{-1})	a^a (Å)	c^a (Å)	$O_{occup}{}^a$	ρ^a (g cm^{-3})	R_{exp} (%)	R_{Bragg} (%)
$Pr(OH)_3$	130.52	6.453(4)	3.769(9)	0.84(8)	4.45	11.6	6.0
1% Eu	83.24	6.453(4)	3.768(9)	0.80(2)	4.39	12.6	7.0
3% Eu	63.05	6.461(1)	3.769(0)	0.66(6)	4.22	13.0	8.5
5% Eu	82.77	6.449(0)	3.763(4)	0.74(5)	4.34	11.9	6.0

[a] Calculated *via* the Rietveld refinement.

The type of dopant and its incorporation influence the properties of the obtained materials to a great extent. Therefore, it is important to determine precisely the amount of the incorporated Eu in $Pr_{1-x}Eu_x(OH)_3$ ($0.01 \leq x \leq 0.05$) nanopowders. In that sense, the ICP analysis was performed and the results reveal that the content of the incorporated Eu is slightly lower than its nominal content for each doped sample (see Table 2).

The morphology of pure and Eu-doped nanostructures was characterized by TEM and FE-SEM. Fig. 2 shows the TEM images of pure and Eu-doped $Pr(OH)_3$ nanostructures, while the SEM images are shown in Fig. S1 in the ESI.† Pure $Pr(OH)_3$ dominantly consists of well-dispersed nanorods with diameters ranging between 5 and 10 nm (Fig. 2(a)). With the increase of the Eu dopant content, the morphology of the obtained nanomaterials changed and besides nanorods, the increasing presence of irregularly shaped grains that do not have the nanorod morphology was also observed. This can be explained

Table 2 Measured Eu content of $Pr_{1-x}Eu_x(OH)_3$ nanostructures by ICP-OES

Sample	Theoretical Eu content (mg g^{-1})	Measured Eu content (mg g^{-1})	Atomic concentration (%)
$Pr_{0.99}Eu_{0.01}(OH)_3$	7.91	6.45	0.82
$Pr_{0.97}Eu_{0.03}(OH)_3$	23.72	20.50	2.59
$Pr_{0.95}Eu_{0.05}(OH)_3$	39.48	32.64	4.13

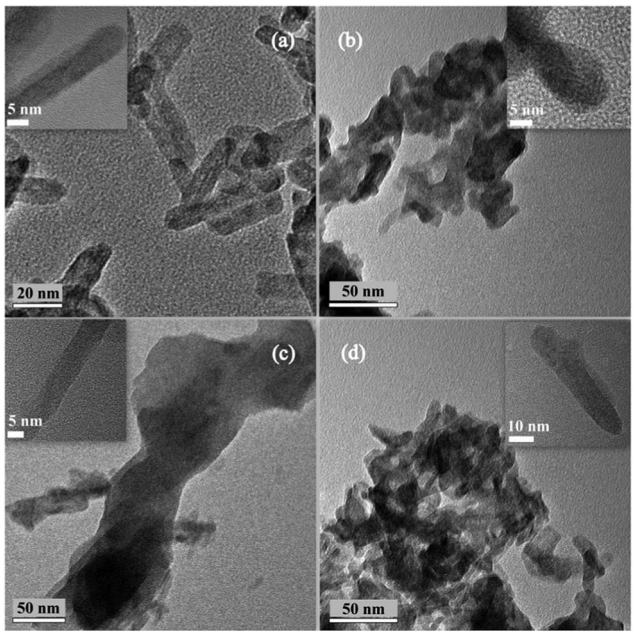

Fig. 2 TEM images of (a) $Pr(OH)_3$, (b) $Pr_{0.99}Eu_{0.01}(OH)_3$, (c) $Pr_{0.97}Eu_{0.03}(OH)_3$, and (d) $Pr_{0.95}Eu_{0.05}(OH)_3$ nanostructures. The insets are the magnified images of individual nanorods.

by the known fact that the dopant atoms can change the crystallization directions and act as the nucleation centers,[17,18] thus changing the resultant morphology of the sample. It is also worth to mention that in the case of the 3% Eu-doped $Pr(OH)_3$ sample, two types of nanorods were formed–narrow nanorods with diameters in the range 7–15 nm (similar to pure $Pr(OH)_3$) and wider nanorods, with diameters of the order of 50 nm (shown in the inset of Fig. S1(c), ESI†).

The nature of the Eu ion incorporation was further studied by Raman spectroscopy through analyzing the influence that Eu doping has on the vibrational properties of the starting material, $Pr(OH)_3$. The crystal symmetry of $Pr(OH)_3$ is hexagonal with a symmetry group $P6_3/m$, for which the group theory predicts 11 Raman active modes: $4A_g$, $2E_{1g}$ and $5E_{2g}$ modes.[19,20] In Fig. 3, the room-temperature Raman spectra of pure and Eu-doped $Pr(OH)_3$ are shown. The main Raman modes of $Pr(OH)_3$ are present in the spectra of the pure and doped samples and are positioned at the energies: 140 cm^{-1} (peak 1), 240 cm^{-1} (peak 2), 294 cm^{-1} (peak 3), 359 cm^{-1} (peak 4), and 465 cm^{-1} (peak 5). The modes positioned at 240 cm^{-1} and 294 cm^{-1} are ascribed to the E_{1g} and E_{2g} lattice vibrations of OH^- anion, whereas the E_{2g} lattice vibrational mode of heavier

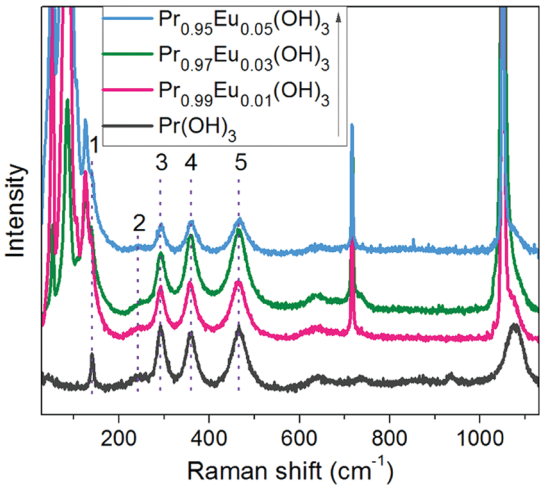

Fig. 3 Room-temperature Raman spectra of $Pr_{1-x}Eu_x(OH)_3$ nanostructures.

Pr^{3+} ions is positioned at a lower energy of 140 cm^{-1}. The vibration frequencies of the OH^- atomic group are positioned at 359 cm^{-1} and 465 cm^{-1} (E_{2g} and E_{1g} modes).[19,20] The Raman peaks 3, 4 and 5 shifted slightly to higher wavenumbers in the $Pr_{0.95}Eu_{0.05}(OH)_3$ spectrum, which can be explained by a certain degree of Eu substitutional incorporation onto the Pr sites as these peaks are positioned at higher wavenumbers in $Eu(OH)_3$ compared to $Pr(OH)_3$.[20] Several low-frequency modes at ~53 cm^{-1}, ~85 cm^{-1}, ~107 cm^{-1}, ~127 cm^{-1}, and ~137 cm^{-1} are present in the Raman spectra of the Eu-doped samples. These modes correspond to nitrates, in the form of either nitrate monohydrate layers interconnected with hydrogen bonds[21,22] or KNO_3.[23,24] Both of these compounds can be formed from the unreacted nitrate ions originating from the precursor. The sharp Raman modes positioned at 715 cm^{-1} and 1050 cm^{-1} correspond to the vibrations of NO_3^- ions.[23,24] Based on the results of Raman spectroscopy and keeping in mind the X-ray diffraction results, we can conclude that some amount of the crystalline KNO_3 phase is present in the Eu-doped $Pr(OH)_3$ samples. The XPS measurements of the $Pr_{1-x}Eu_x(OH)_3$ samples enabled the elucidation of changes in the chemical composition and electronic structures with Eu doping and determined the valence states of various species present in the pure and doped samples.

Fig. 4(a) shows the survey XPS spectra of the $Pr_{1-x}Eu_x(OH)_3$ samples, while the Pr 3d, Eu 3d, O 1s, and K 2p/C 1s XPS spectra are shown in Fig. 4(b). The Pr 3d spectra (Fig. 4(b), upper left) contain two spin–orbit doublets, labeled c/c' and b/b' with approximate energies of 929/949 eV and 933/954 eV, respectively. These doublets represent the $3d_{5/2}$ (c, b) and $3d_{3/2}$ (c', b') components of the Pr 3d spectra. An additional structure t is present in the $3d_{3/2}$ component and its presence can be explained by multiple effects. The doublets c/c' and b/b' are found both in Pr^{4+} and Pr^{3+}, so they cannot be used to distinguish between these two valence states of Pr. The small peaks observed at ~923 eV and ~943 eV are identified as X-ray satellites, originating from the non-monochromatic X-ray source. From the Eu 3d spectra (Fig. 4(b), upper right), we can observe that the

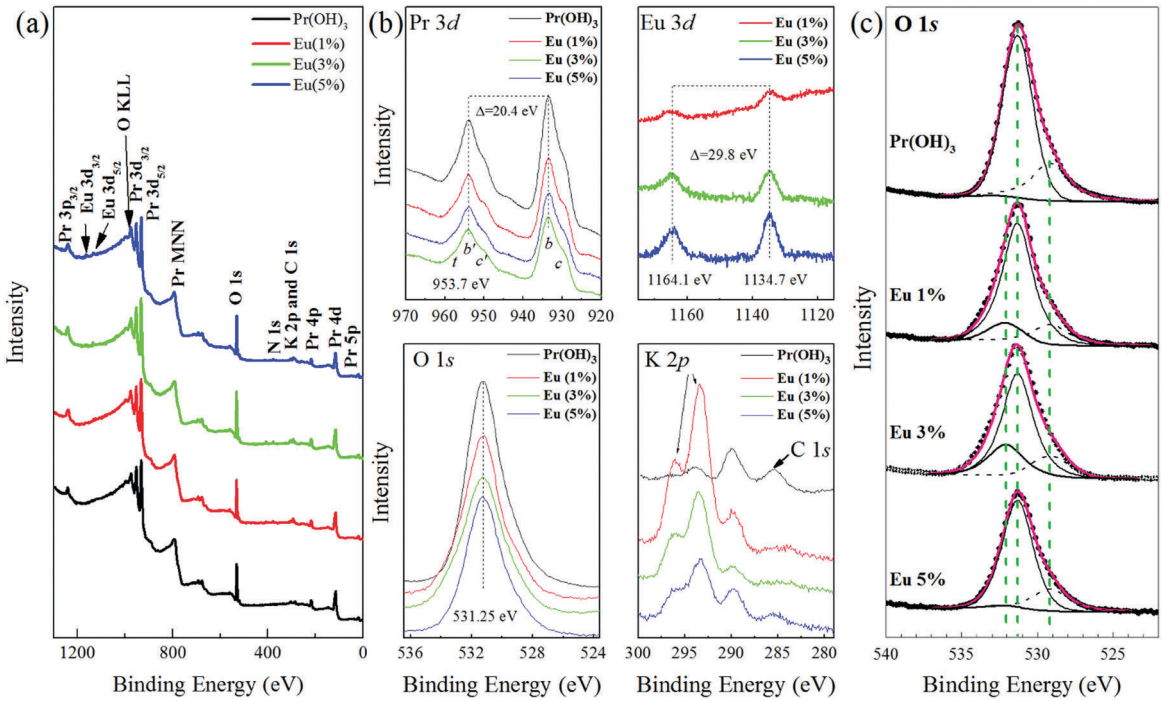

Fig. 4 XPS spectra of $Pr_{1-x}Eu_x(OH)_3$ nanostructures: (a) survey spectra, (b) high-resolution spectra of Pr 3d, Eu 3d, O 1s and K 2p/C 1s regions and (c) deconvolution of O 1s region into three peaks.

components Eu $3d_{5/2}$ and $3d_{3/2}$ are positioned at ~1134.7 eV and ~1164.1 eV, respectively. These values correspond to the Eu^{3+} valence state. When compared to the literature values for Eu_2O_3 (1133.7),[25] $Eu(OH)_3$ (1134.3)[26] and $Eu(NO_3)_3$ (1136.4),[25] it can be observed that these peaks are closest to those of $Eu(OH)_3$, which confirms the substitutional incorporation of Eu^{3+} and the absence of europium oxide/nitrate. More evidence indicating that Eu_2O_3 is not present in these samples is the fact that the strong Raman mode of Eu_2O_3 at ~330 cm^{-1} was not registered in the Raman spectra. The K 2p states are particularly prominent in the 1% and 3% Eu-doped samples (see Fig. 4(b)) and originate from the KNO_3 phase, as already observed in the XRD and Raman spectra of the doped samples. A low-intensity C 1s peak (see Fig. 4(b)) originates from the surface impurity carbons, while the N1s states are characterized by very low-intensity peaks visible in the survey XPS spectra. The O 1s peaks of $Pr_{1-x}Eu_x(OH)_3$ samples (Fig. 4(c)) are asymmetric and have been deconvoluted into three components positioned at ~529 eV, ~531 eV, and ~532 eV. The vertical dashed lines shown in Fig. 4(c) indicate the binding energy (BE) position of these three components. The latter two are generally ascribed to the lattice oxygen and adsorbed –OH groups, possibly from water,[25–27] while the peak at ~529 eV can be ascribed to the surface oxygen vacancies.[20]

The elemental composition of the investigated samples obtained by XPS measurements is represented in Table 3. The atomic concentrations, shown in Table 3, were obtained considering the sensitivity factors of PHI (Physical Electronics) and the peak features of $Pr(3d_{5/2})$, O(1s) and $Eu(3d_{5/2})$ (Fig. 4). It can be noticed that the relative atomic concentrations of Eu, calculated as Eu/(Eu + Pr), were higher than the nominal stoichiometric concentrations of this element. This can be a consequence of the segregation of the dopant atoms on the materials surface as already registered by XPS in other rare earth nanocomposites.[28] This finding suggests that Eu^{3+} ions are segregated at the surfaces of nanocrystals, but mostly connected to oxygen ions as deduced from the Eu 3d binding energies. From the peak area fitting data of the components that belong to lattice oxygen and oxygen vacancies, we have calculated the oxygen molar ratio, which is also summarized in Table 3. Although XPS provides the information about the surface stoichiometry, the obtained ratio is in agreement with the XRD results (see Table 1), confirming that the Eu-doped samples are more oxygen deficient.

Table 3 Elemental composition of $Pr(OH)_3$, pure and Eu-doped as determined by XPS

	Atomic concentration (%)				
Sample	Pr	O	Eu	Eu/(Eu+Pr)	Vacancy/lattice
$Pr(OH)_3$	24.501	75.499	0.000		0.16
1% Eu	21.674	77.846	0.480	2.0%	0.20
3% Eu	19.189	78.369	2.441	11.3%	0.22
5% Eu	21.213	75.030	3.757	15.0%	0.26

Infrared spectroscopy (IR) was employed to evidence the presence of the –OH groups as well as other organic and inorganic species. The IR transmission spectra of the pure and Eu-doped $Pr(OH)_3$, obtained in the range 500–4000 cm^{-1}, are shown in Fig. 5. The peak at 670 cm^{-1} represents the Pr–O–H lattice vibration.[13,20] The prominent broad peaks at 1382 cm^{-1}

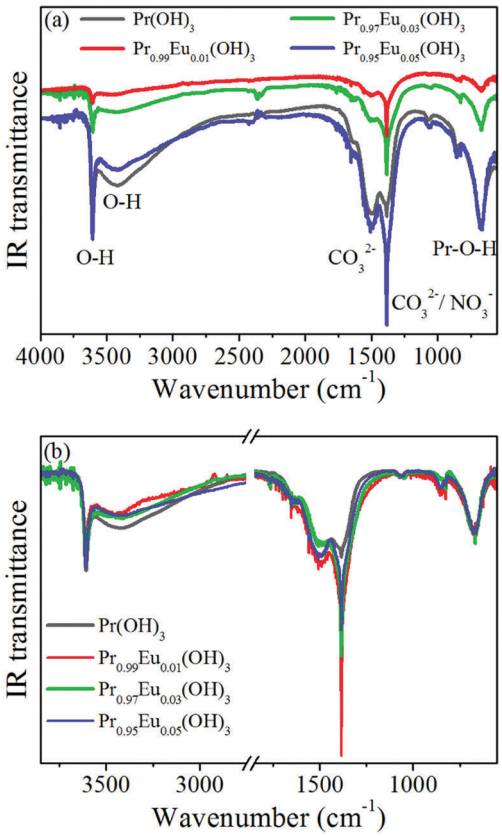

Fig. 5 (a) IR transmission spectra and (b) normalized IR spectra of pure and Eu-doped $Pr(OH)_3$ nanostructures.

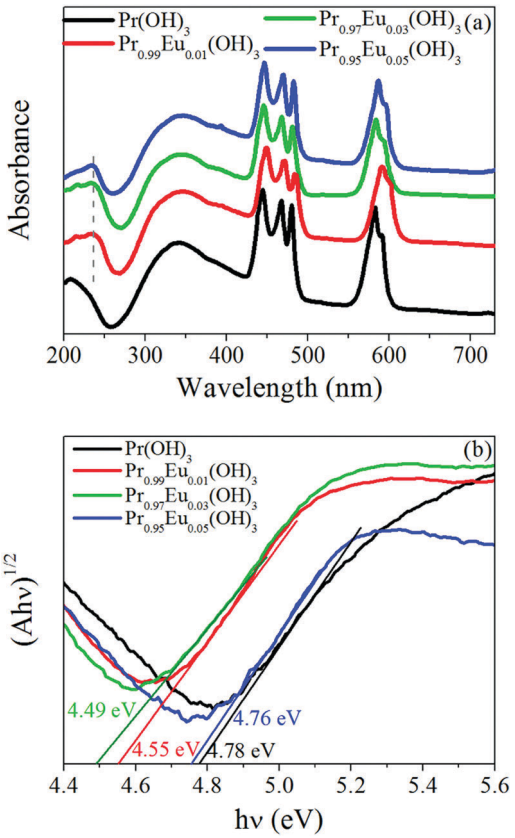

Fig. 6 (a) Absorption spectra and (b) Tauc plots of $(Ah\nu)^{1/2}$ *vs.* $(h\nu)$ for $Pr_{1-x}Eu_x(OH)_3$ nanostructures.

and 1505 cm^{-1} belong to the symmetric and asymmetric COO^- vibrations[29] due to the adsorbed carbon species. Another sharp peak at 1385 cm^{-1} with a much higher intensity in the spectra of the doped samples is observed. This sharp peak can be ascribed to the NO_3^- vibrations[30] together with the observed low-intensity peak at ~828 cm^{-1}, which also corresponds to the NO_3^- vibrations and is present only in the doped samples.[30] The intensity of this sharp peak (1385 cm^{-1}) is very high in the 1% Eu-doped sample and decreases with the increase in the dopant concentration as shown in the normalized IR spectra in Fig. 5(b) (normalized to the Pr–OH vibration peak), which is in agreement with the XPS K 2p spectra of the pure and doped samples. Another sharp peak at 3600 cm^{-1} represents the vibrations of the OH^- groups from $Pr(OH)_3$/$Eu(OH)_3$, while the broad peak at 3400 cm^{-1} corresponds to the delocalized OH^- vibrations from the adsorbed H_2O on the sample surface.[29,31]

The UV-vis absorption spectra of $Pr_{1-x}Eu_x(OH)_3$ are presented in Fig. 6(a). A strong absorption band can be observed in the region below 270 nm, corresponding to the band gap, and is shifted to a lower wavelength for the Eu-doped samples compared to that in the $Pr(OH)_3$ spectrum. Several sharper peaks at 446 nm, 462 nm, 470 nm, 583 nm and 591–597 nm represent the Pr^{3+} electronic transitions. These peaks were observed in both pure and doped samples.

There are no peaks that can be ascribed to the intraband 4f–4f Eu^{3+} electronic transitions due to the fact that the doping percentage is low. Another very broad absorption peak at ~340 nm can be ascribed to the formation of oxygen-vacancy impurity levels within the band gap. These states are already seen in the defective $La(OH)_3$ nanorods (with the absorption around 280 nm) and ascribed to the surface oxygen vacancy states formed during the synthesis process.[3]

From the absorption spectra shown in Fig. 6(a), by applying the absorption spectra fitting method for the indirect electronic transitions,[32] the band gap of these materials was estimated. Fig. 6(b) presents the Tauc plots[33] for the indirect transition of the $Pr_{1-x}Eu_x(OH)_3$ samples. It was deduced that the pure $Pr(OH)_3$ band gap of ~4.78 eV was shifted to ~4.5 eV in $Pr_{0.99}Eu_{0.01}(OH)_3$ and $Pr_{0.97}Eu_{0.03}(OH)_3$, while it increased again in $Pr_{0.95}Eu_{0.05}(OH)_3$, approaching the $Pr(OH)_3$ value. The lower gap of the 1% and 3% Eu-doped samples can be explained by the presence of a higher amount of the KNO_3 phase in these samples, which have a lower band gap[14,34] compared to that of $Pr(OH)_3$.

In order to probe the intraband defect states, the PL measurements were performed using a 340 nm excitation light with the purpose of exciting the states corresponding to the broad peak centered at 340 nm in the absorption spectra (see Fig. 6(a)). The PL spectra of $Pr_{1-x}Eu_x(OH)_3$ samples shown in Fig. S2 (ESI†) consist of an intense PL peak centered at 430 nm and several lower intensity Pr^{3+} emission peaks that are red-shifted, compared to those of their counterparts in the

absorption spectra. The characteristic Eu^{3+} peaks are not observed because of the presence of the hydroxyl groups, which act as the luminescence quenching centers and can increase the non-radiative processes.[35] The intensive blue emission peak can be attributed to the deep level oxygen vacancy defect states and originates from the recombination of an electron occupying the vacancy and the photogenerated holes.[3,36] The intensity of this peak increases in the 3% and 5% Eu-doped samples. This is in accordance with the XPS and XRD results, which showed that the oxygen deficiency increased with increased Eu content.

Although the determined band gap values of $Pr_{1-x}Eu_x(OH)_3$ nanostructures are relatively high, the sub-band gap state observed from the PL and UV-vis absorption spectra (see Fig. 6(a) and Fig. S2, ESI†) allows for these structures to be tested as the potential photocatalysts in the UV region. Therefore, the photocatalytic degradation of the RO16 dye was tested for $Pr_{1-x}Eu_x(OH)_3$ nanostructures under UV light.

The kinetics of the degradation of RO16 under UV light is shown in Fig. 7(a). It is evident that RO16 can be effectively removed by the $Pr_{1-x}Eu_x(OH)_3$ nanostructures. The pure $Pr(OH)_3$ sample showed a moderate adsorption in the dark and its photocatalytic removal efficiency was more than 90% after 180 min. A pronounced adsorption in the equilibrium period of 60 min before the exposure to UV light was seen in the 3% Eu-doped sample. On the contrary, the 1% and 5% Eu-doped samples showed no adsorption. The iso-electric point of a photocatalyst influences the adsorption process to a great extent. Therefore, the zeta potentials for pure, 1%, and 3% Eu-doped $Pr(OH)_3$ (shown in Fig. 8(b)) were measured in the pH range of 2.0–12.0 and their iso-electric points were 8.2, 7.6 and 8.8 respectively. At pH = 4.7, which was the natural pH value of the solution, the surface charge of the catalysts is positive in the following order: 3% Eu > $Pr(OH)_3$ > 1% Eu. As the RO16 dye molecule is negatively charged, the best adsorption is expected in the 3% Eu-doped sample due to the stronger electrostatic interaction between the adsorbent and the adsorbate. A slightly weaker adsorption is expected in $Pr(OH)_3$ and the lowest is in the 1% Eu-doped $Pr(OH)_3$ sample. This is in good agreement with the experimental results. The changes in the morphology of the 3% Eu-doped $Pr(OH)_3$ (*i.e.* the existence of two types of nanorods with diameters of the orders of magnitude ~10 nm and ~50 nm as shown in Fig. S1(c), ESI†) and the increased amount of oxygen vacancies (deduced from the Rietveld analysis) in this sample can be additional reasons for the enhanced adsorption.

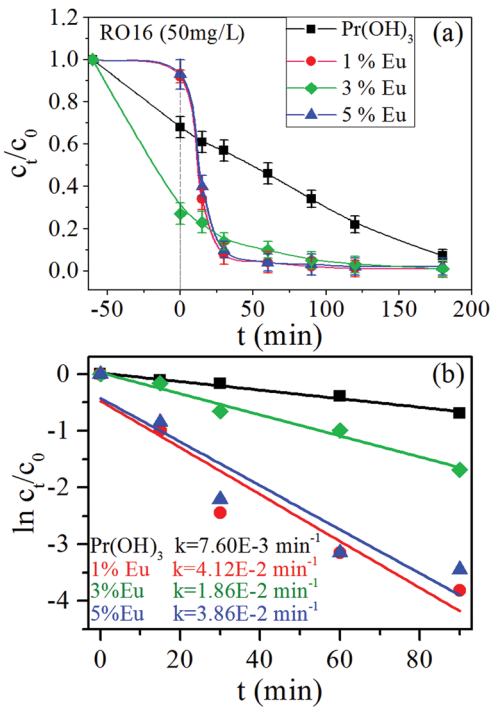

Fig. 7 (a) Degradation of RO16 dye under UV light in the presence of the pure and Eu-doped $Pr(OH)_3$ nanostructures and (b) the first-order reaction kinetics and constant *k* values.

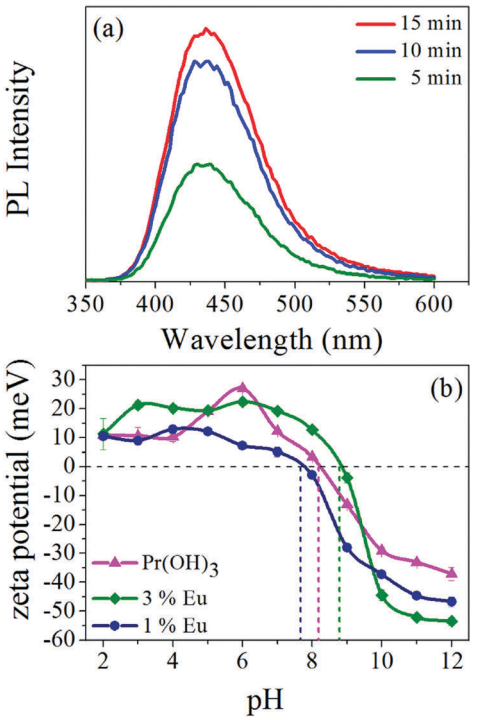

Fig. 8 (a) PL spectral changes observed during UV illumination of the $Pr_{0.95}Eu_{0.05}(OH)_3$ sample in the solution of terephthalic acid after 5, 10, and 15 min and (b) zeta potential dependence on pH value for pure, 1%, and 3% Eu-doped $Pr(OH)_3$.

The Eu-doped $Pr(OH)_3$ nanostructures exhibited a much faster removal efficiency than pure $Pr(OH)_3$ and a faster dye removal at the beginning of the reaction (Fig. 7(a)). A rapid removal of RO16 was observed in the first 30 min and after 70 min, the dye was almost completely removed. Under the similar conditions, the Eu-doped $Pr(OH)_3$ nanostructures demonstrated a much better photocatalytic activity than Degussa.[37,38] The photocatalytic degradation of RO16 followed the first-order kinetics (Fig. 7(b)), expressed by the equation $\ln(C/C_0) = kt$, where C_0 is the initial dye concentration and C is the dye concentration at time t. The first-order rate constant k values, obtained from the slope of $\ln(C/C_0)$ *vs.* t, for the $Pr_{1-x}Eu_x(OH)_3$ samples are presented in Fig. 7(b).

It can be deduced that the Eu-doped samples have significantly higher k values than that of pure $Pr(OH)_3$, confirming that these samples are better photocatalysts than the pure $Pr(OH)_3$ sample.

The XRD, XPS and UV-vis absorption spectra have revealed that the $Pr_{1-x}Eu_x(OH)_3$ samples are oxygen deficient. In addition, the XRD results have confirmed that the oxygen deficiency increases with Eu doping. The XPS measurements suggested the high segregation of Eu ions on the surface of the doped nanostructures. The presence of lattice defects such as oxygen vacancies (V_O) and Eu^{3+} ions, particularly on the surface of Eu-doped nanostructures, can influence, to a great extent, the photocatalytic activity of the $Pr_{1-x}Eu_x(OH)_3$ samples.

The photo-generated electrons or holes can be captured by V_O, which forms impurity levels inside the band gap and serves as charge carrier trap, suppressing the e–h recombination process.[39] Moreover, the vacancies facilitate the charge transfer to the adsorbed species on the catalyst surface such as O_2 or H_2O, forming reactive radicals (superoxide radical ($O_2^{\bullet -}$) or $OH^{\bullet}$), the existence of which is important for a fast and successful photocatalytic degradation of organic dyes. It is well-documented that at the surface of oxide nanostructures such as TiO_2 or CeO_2, water dissociation takes place exclusively on the oxygen vacancy defect sites, where every surface V_O enables the formation of two hydroxyl groups.[40–43] The infrared study of $Pr_{1-x}Eu_x(OH)_3$ nanostructures confirmed the presence of hydroxyl groups from water.

The formation of the $OH^{\bullet}$ radicals was tested on the surface of the $Pr_{0.95}Eu_{0.05}(OH)_3$ photocatalyst under UV irradiation and detected by the PL method. The PL spectra of the reaction solution were measured at room temperature and are presented in Fig. 8(a). Terephthalic acid reacts with the $OH^{\bullet}$ radicals producing 2-hydroxyterephthalic acid, which exhibits a PL peak at 425 nm.[44] The intensity of this peak is proportional to the amount of $OH^{\bullet}$ radicals produced in the solution.[44,45] As shown in Fig. 8(a), a substantial increase of the intensity of the 425 nm peak with prolonged illumination time indicates the increasing amount of $OH^{\bullet}$ radicals produced at the surface of the $Pr_{0.95}Eu_{0.05}(OH)_3$ sample.

The existence of the surface and subsurface vacancies also enables better adsorption of O_2, which can capture the photogenerated electrons or electrons located on V_O, producing the superoxide radical groups.[41,46] In addition, due to a high oxidative potential of the holes, they can directly attack the dye, leading to its oxidation (h^+ + dye → $dye^{\bullet +}$ → oxidation of the dye). Furthermore, the photogenerated holes can easily react with the surface-bound H_2O or hydroxyls (OH^-), forming the hydroxyl radicals ($OH^{\bullet}$). Although similar studies, to the best of our knowledge, have not been performed for the $Pr(OH)_3$ nanostructures, it is reasonable to assume that the oxygen vacancies have an important role in the photocatalytic process at the $Pr_{1-x}Eu_x(OH)_3$ surface. Furthermore, the recent papers of Dong *et al.*[3] and Wang *et al.*,[11] aimed at the investigation of the photocatalytic properties of the defective $La(OH)_3$ nanorods and $La(OH)_3$ nanorods doped with 4f elements, demonstrated the crucial role of oxygen vacancies in the photocatalytic degradation of dyes and strongly support our findings. The oxygen vacancy states in the band gap were registered by the PL and absorption measurements.

Moreover, Eu^{3+} ions are often used as the dopants that can prevent rapid recombination of the photogenerated electrons and holes because they create the surface states that present a barrier for electrons.[47] The emission from these states was not observed in the PL spectra excited with 340 nm probably due to the OH bond quenching. However, since the Eu^{3+} states were registered by XPS, they can be responsible for the enhanced photocatalytic activity of the Eu-doped nanostructures due to the abovementioned electron trapping effect.

In the recent paper of Mahlalela *et al.*, it was demonstrated that TiO_2 nanoparticles exhibited an enhanced photocatalytic activity in the presence of KNO_3. This was ascribed to the increased production of the hydroxyl radicals due to the presence of NO_3^- anions. The direct photolysis of nitrate ions (NO_3^-) during irradiation with $\lambda > 280$ nm can result in the formation of the $NO_2^{\bullet}$ and $O^{\bullet -}$ radicals. In the presence of water, the $O^{\bullet -}$ radicals can be protonated, leading to the formation of the hydroxyl radicals ($OH^{\bullet}$) and OH^- ions according to the following reaction:[48]

$$(NO_3^-) \xrightarrow{h} (NO_3^-)^* \rightarrow NO_2^{\bullet} + O^{\bullet -} + H_2O \rightarrow NO_2^{\bullet} + OH^{\bullet} + OH^- \quad (1)$$

In this way, the concentration of the $OH^{\bullet}$ radicals is increased, thus enhancing the photodegradation of the dyes. Furthermore, nitrate ions are good acceptors for the photoinduced electrons, forming the nitrogen trioxide anion radicals ($NO_3^{\bullet 2-}$). These radicals on reacting with water would form powerful nitrogen dioxide ($NO_2^{\bullet}$) anions, which are capable of oxidizing the dyes.[48]

The XPS, XRD and Raman analysis confirmed the presence of the KNO_3 phase in the Eu-doped samples. The presence of NO_3^- ions at the surface of the doped samples can additionally improve their photocatalytic properties due to the abovementioned radical formation. Considering all previously mentioned results, a mechanism of photocatalytic reactions in Eu-doped $Pr(OH)_3$ is proposed and presented in Fig. 9.

The photocatalytic stability was tested on the $Pr_{0.95}Eu_{0.05}(OH)_3$ sample. Fig. S3 (ESI†) shows the repeated photocatalytic runs under the UV light irradiation. Although there was a certain drop in the efficiency in the second run, these results indicated that the Eu-doped $Pr(OH)_3$ catalysts were stable. The drop in the efficiency after the first run is ascribed to the adsorbed dye molecules and the reduction of a number of the active sites since the catalyst is recycled by centrifugation and deionized water washing without any additional chemical treatment.

Therefore, an enhanced photocatalytic activity of the Eu-doped $Pr(OH)_3$ nanostructures can be explained by the presence of oxygen vacancies, Eu^{3+} trapping states and KNO_3-mediated hydroxyl radical production at the surface of our as-prepared samples. The synergy of these three factors resulted in the efficient separation of the photogenerated electrons and holes and their transfer to adsorbed species at the surface, thus enabling excessive formation of the reactive radicals and efficient dye degradation.

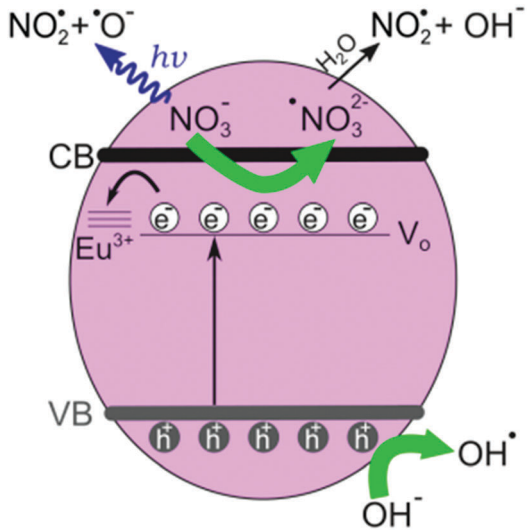

Fig. 9 Illustration of the photocatalytic mechanism of Eu-doped $Pr(OH)_3$ under the UV light irradiation.

This study provides a new insight into the role of oxygen vacancies, 4f dopants and a proper choice of alkaline metal hydroxides in promoting the photocatalytic efficiency of $Pr(OH)_3$. Our future studies would be dedicated to the investigation of the influence of other 4f dopants on the morphology, the electronic structure and the photocatalytic performances of $Pr(OH)_3$ nanostructures.

Conclusions

In summary, the defective $Pr_{1-x}Eu_x(OH)_3$ nanostructures were synthesized by a simple microwave-assisted hydrothermal method and the comprehensive characterization has been performed by XRD, XPS, ICP-OES, FE-SEM, Raman, IR and DR spectroscopy. It is observed that Eu^{3+} doping promotes the formation of oxygen vacancies and changes the morphology of $Pr(OH)_3$ nanorods. Eu^{3+} ions also have a tendency to segregate at the surface of the nanostructure. Furthermore, the presence of KNO_3 phase is registered in the doped samples. The Eu-doped nanostructures exhibit an excellent photocatalytic activity towards the photodegradation of an azo dye compared to that of pure $Pr(OH)_3$ nanorods. Oxygen vacancies, the change in the morphology and the presence of Eu^{3+} and NO_3^- ions at the $Pr(OH)_3$ surface play a significant role in improving the photocatalytic properties of the $Pr(OH)_3$ nanostructures. The enhanced photocatalytic activity of the $Pr_{1-x}Eu_x(OH)_3$ nanostructures originates from the combined effect of oxygen vacancies and Eu^{3+} ions, which act as trapping centres, subsequently enabling the facile charge transfer to the adsorbed species. In this way, a fast electron–hole recombination can be suppressed and more reactive radicals can be formed. The presence of the KNO_3 phase in the $Pr_{1-x}Eu_x(OH)_3$ samples additionally improves the photocatalytic performances of $Pr(OH)_3$ nanostructures, *i.e.*, the presence of NO_3^- ions can enhance the production of $NO_2^{\bullet}$ and $OH^{\bullet}$ radicals. Furthermore, the 3% Eu-doped sample exhibited very good adsorption properties due to a higher electrostatic attraction of anionic dye and different morphology compared to those of other samples. The possibility of tuning the ratio of photocatalytic *versus* adsorptive activity of the Eu-doped $Pr(OH)_3$ nanostructures makes them desirable for environmental applications.

Conflicts of interest

There are no conflicts of interest to declare.

Acknowledgements

This work was supported by Serbian Ministry of Education, Science and Technological Development under projects OI 171032 and III 45018. V. D. Araújo and M. I. B. Bernardi wish to thank Brazilian agencies FAPESP, FACEPE, and CNPq for the financial support. The authors wish to thank Prof. Tamara Radetic for TEM images, Dr Aleksandar Matković and MSc Marijana Milićević for SEM images and to Dr Nenad Tadić for DRS measurements.

References

1 X. Wang and Y. Li, *Chem. – Eur. J.*, 2003, **9**, 5627–5635.
2 X. Ouyang, S. Yuan, Q. Qiu, W. Zeng, G. A. Hope and H. Li, *Inorg. Chem. Commun.*, 2014, **46**, 21–23.
3 F. Dong, X. Xiao, G. Jiang, Y. Zhang, W. Cui and J. Ma, *Phys. Chem. Chem. Phys.*, 2015, **17**, 16058–16066.
4 D. Zhang, T. Yan, L. Shi, H. Li and J. F. Chiang, *J. Alloys Compd.*, 2010, **506**, 446–455.
5 S. Zhang and C. Yao, *Mater. Lett.*, 2013, **94**, 143–146.
6 X. Sun, T. Zhai, X. Lu, S. Xie, P. Zhang, C. Wang, W. Zhao, P. Liu and Y. Tong, *Mater. Res. Bull.*, 2012, **47**, 1783–1786.
7 T. Zhai, S. Xie, X. Lu, L. Xiang, M. Yu, W. Li, C. Liang, C. Mo, F. Zeng, T. Luan and Y. Tong, *Langmuir*, 2012, **28**, 11078–11085.
8 J. Tang, J. Chen, W. Huang, D. Li, Y. Zhu, Y. Tong and Y. Zhang, *Chem. Eng. J.*, 2014, **252**, 202–209.
9 A. Dodd, *J. Colloid Interface Sci.*, 2013, **392**, 137–140.
10 X. Wang and Y. Li, *Angew. Chem., Int. Ed.*, 2002, **41**, 4790–4793.
11 Y. Wang, S. Liu, Y. Cai, S. Deng, B. Han, R. Han, Q. Li and Y. Wang, *Ceram. Int.*, 2014, **40**, 5091–5095.
12 A. C. Larson and R. B. Von Dreele, *Report LAUR 86-748*, Los Alamos National Laboratory, 2004.
13 D. F. Mullica, W. O. Milligan and G. W. Beall, *J. Inorg. Nucl. Chem.*, 1979, **41**, 525–532.
14 M. Hafez, I. S. Yahia and S. Taha, *Acta Phys. Pol., A*, 2015, **127**, 734–740.
15 R. Shannon, *Acta Crystallogr., Sect. A: Found. Crystallogr.*, 1976, **32**, 751–767.
16 S. Deshpande, S. Patil, S. V. N. T. Kuchibhatla and S. Seal, *Appl. Phys. Lett.*, 2005, **87**, 133113.

17 J. D. Bryan and D. R. Gamelin, *Prog. Inorg. Chem.*, John Wiley & Sons, Inc., 2005, ch. 2, pp. 47–126, DOI: 10.1002/0471725560.
18 C. Li, H. Liu and J. Yang, *Nanoscale Res. Lett.*, 2015, **10**, 1–6.
19 K. Ahrens, H. Gerlinger, H. Lichtblau, G. Schaack, G. Abstreiter and S. Mroczkowski, *J. Phys. C: Solid State Phys.*, 1980, **13**, 4545.
20 J.-G. Kang, Y. Jung, B.-K. Min and Y. Sohn, *Appl. Surf. Sci.*, 2014, **314**, 158–165.
21 R. M. Escribano, D. Fernández-Torre, V. J. Herrero, B. Martín-Llorente, B. Maté, I. K. Ortega and H. Grothe, *Vib. Spectrosc.*, 2007, **43**, 254–259.
22 H. Grothe, C. E. Lund Myhre and C. J. Nielsen, *J. Phys. Chem. A*, 2006, **110**, 171–176.
23 M. H. Brooker, *Can. J. Chem.*, 1977, **55**, 1242–1250.
24 D. Liu, F. G. Ullman and J. R. Hardy, *Phys. Rev. B: Condens. Matter Mater. Phys.*, 1992, **45**, 2142–2147.
25 F. Mercier, C. Alliot, L. Bion, N. Thromat and P. Toulhoat, *J. Electron Spectrosc. Relat. Phenom.*, 2006, **150**, 21–26.
26 H. Wu, Y. Zhang, M. Zhou, C. Yao and X. Ge, *Cryst. Res. Technol.*, 2016, **51**, 508–512.
27 J.-C. Dupin, D. Gonbeau, P. Vinatier and A. Levasseur, *Phys. Chem. Chem. Phys.*, 2000, **2**, 1319–1324.
28 N. Paunovic, Z. Dohcevic-Mitrovic, R. Scurtu, S. Askrabic, M. Prekajski, B. Matovic and Z. V. Popovic, *Nanoscale*, 2012, **4**, 5469–5476.
29 J.-G. Kang, Y.-I. Kim, D. Won Cho and Y. Sohn, *Mater. Sci. Semicond. Process.*, 2015, **40**, 737–743.
30 J. T. Kloprogge and R. L. Frost, Infrared and Raman spectroscopic studies of layered double hydroxides (LDHs), in *Layered double hydroxides: Present and future*, ed. V. Rives, Nova Science Publishers, Inc., New York, 2001, pp. 139–192.
31 F. Cui, J. Zhang, T. Cui, S. Liang, L. Ming, Z. Gao and B. Yang, *Nanotechnology*, 2008, **19**, 065607.
32 N. Ghobadi, *Int. Nano Lett.*, 2013, **3**, 2.
33 M. Wang, P. Guo, T. Chai, Y. Xie, J. Han, M. You, Y. Wang and T. Zhu, *J. Alloys Compd.*, 2017, **691**, 8–14.
34 M. K. Aydinol, J. V. Mantese and S. P. Alpay, *J. Phys.: Condens. Matter*, 2007, **19**, 496210.
35 Z. Zuo, D. Liu, J. Liu, H. Liu, S. Qin and F. Zheng, *Mater. Chem. Phys.*, 2010, **123**, 502–506.
36 D. Liu, Y. Lv, M. Zhang, Y. Liu, Y. Zhu, R. Zong and Y. Zhu, *J. Mater. Chem. A*, 2014, **2**, 15377–15388.
37 D. Mijin, M. Radulović, D. Zlatić and P. Jovančić, *Chem. Ind. Chem. Eng. Q.*, 2007, **13**, 179–185.
38 R. C. Hsiao, L. S. Roselin, H.-L. Hsu, R. Selvin and R. S. Juang, *Int. J. Mat. Eng. Innov.*, 2011, **2**, 96–108.
39 F. Kayaci, S. Vempati, I. Donmez, N. Biyikli and T. Uyar, *Nanoscale*, 2014, **6**, 10224–10234.
40 R. Schaub, P. Thostrup, N. Lopez, E. Lægsgaard, I. Stensgaard, J. K. Nørskov and F. Besenbacher, *Phys. Rev. Lett.*, 2001, **87**, 266104.
41 X. Pan, M.-Q. Yang, X. Fu, N. Zhang and Y.-J. Xu, *Nanoscale*, 2013, **5**, 3601–3614.
42 Z. Yang, Q. Wang, S. Wei, D. Ma and Q. Sun, *J. Phys. Chem. C*, 2010, **114**, 14891–14899.
43 N. M. Tomić, Z. D. Dohčević-Mitrović, N. M. Paunović, D. Ž. Mijin, N. D. Radić, B. V. Grbić, S. M. Aškrabić, B. M. Babić and D. V. Bajuk-Bogdanović, *Langmuir*, 2014, **30**, 11582–11590.
44 K.-i. Ishibashi, A. Fujishima, T. Watanabe and K. Hashimoto, *Electrochem. Commun.*, 2000, **2**, 207–210.
45 T.-M. Su, Z.-L. Liu, Y. Liang, Z.-Z. Qin, J. Liu and Y.-Q. Huang, *Catal. Commun.*, 2012, **18**, 93–97.
46 C. L. Muhich, Y. Zhou, A. M. Holder, A. W. Weimer and C. B. Musgrave, *J. Phys. Chem. C*, 2012, **116**, 10138–10149.
47 D. Yue, D. Chen, W. Lu, M. Wang, X. Zhang, Z. Wang and G. Qian, *RSC Adv.*, 2016, **6**, 81447–81453.
48 L. C. Mahlalela and L. N. Dlamini, *Surf. Interfaces*, 2016, **1–3**, 21–28.